

Intertwined Quantum Phase Transitions in Bose and Bose-Fermi Systems

A. Leviatan

Racah Institute of Physics, The Hebrew University, Jerusalem 91904, Israel

E-mail: ami@phys.huji.ac.il

Abstract. Pronounced structural changes within individual configurations (Type I QPT), superimposed on an abrupt crossing of these configurations (Type II QPT), define the notion of intertwined quantum phase transitions (QPTs). We discuss and present evidence for such a scenario in finite Bose and Bose-Fermi systems. The analysis is based on algebraic models with explicit configuration mixing, where the two types of QPTs describe shape-phase transitions in-between different dynamical symmetries and shape-coexistence with crossing.

1 Introduction

Quantum phase transitions (QPTs) are qualitative changes in the properties of a physical system induced by variation of parameters in the Hamiltonian [1, 2]. They occur at zero temperature hence are driven by quantum fluctuations and their study is currently a topic of great interest in diverse fields [3]. Such ground-state phase transitions can be categorized into two types. The first, denoted Type I QPT, is a phase transition in a single configuration [4], described by an Hamiltonian of the form [5],

$$\hat{H}(\xi) = (1 - \xi)\hat{H}_1 + \xi\hat{H}_2, \quad (1)$$

where the separate Hamiltonians \hat{H}_1 and \hat{H}_2 are non-commuting, act in the same Hilbert space (\mathcal{H}) and correspond to different phases of the system. When the control parameter ξ changes from 0 to 1, the spectra and eigenstates of $\hat{H}(\xi)$ progress from those of \hat{H}_1 to those of \hat{H}_2 . The number of basis states is preserved throughout the transition. A schematic illustration of the evolving spectra in a Type I QPT is shown in Fig. 1(a).

A second type of phase transition, denoted Type II QPT, occurs when two (or more) configurations coexist [6]. In this case, the quantum Hamiltonian can be cast in matrix form [7],

$$\hat{H}(\xi_A, \xi_B, \omega) = \begin{bmatrix} \hat{H}_A(\xi_A) & \hat{W}(\omega) \\ \hat{W}(\omega) & \hat{H}_B(\xi_B) \end{bmatrix}, \quad (2)$$

where the indices A and B denote the two configurations. The terms,

$$\hat{H}_A(\xi_A) = (1 - \xi_A)\hat{H}_{A;1} + \xi_A\hat{H}_{A;2}, \quad (3a)$$

$$\hat{H}_B(\xi_B) = (1 - \xi_B)\hat{H}_{B;1} + \xi_B\hat{H}_{B;2}, \quad (3b)$$

act in different Hilbert spaces (\mathcal{H}_A and \mathcal{H}_B), and the mixing term $\hat{W}(\omega)$ connects the two spaces. As the control parameters (ξ_A, ξ_B, ω) are varied, each of the sub-Hamiltonians, $\hat{H}_A(\xi_A)$ and $\hat{H}_B(\xi_B)$, can undergo a QPT of Type I, and the combined Hamiltonian $\hat{H}(\xi_A, \xi_B, \omega)$, which acts in the enlarged

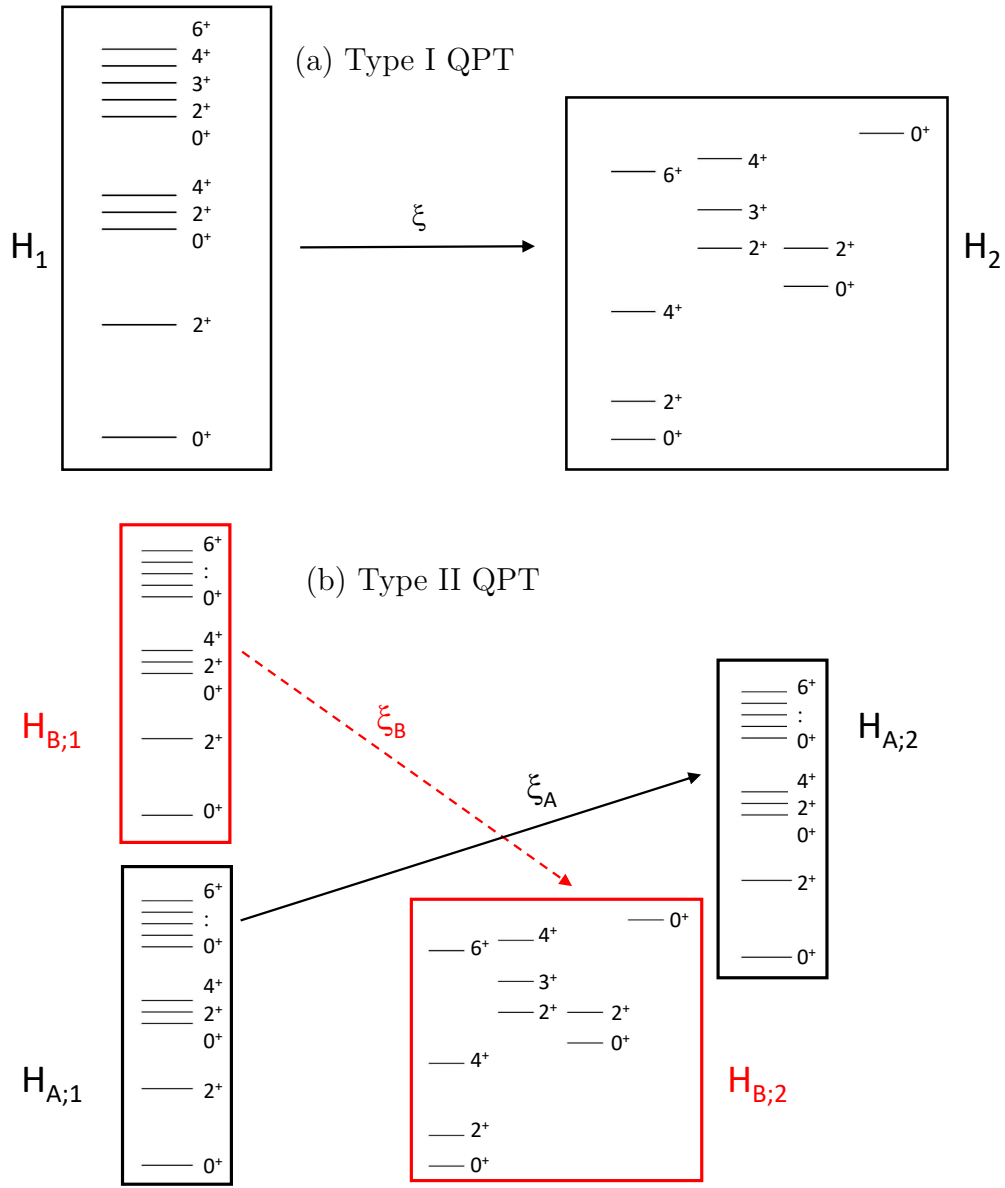


Figure 1: Schematic illustration for the evolution of structure in a quantum phase transition (QPT). (a) Type I QPT, Eq. (1), portraying a change from spherical-vibrator to deformed-rotor spectra within the Hilbert space of a single configuration. (b) Type II QPT, Eq. (2), portraying a coexistence and crossing of sets of levels associated with different configurations (A and B). When both types of QPTs are distinguishable, they define intertwined QPTs in the extended Hilbert space.

Hilbert space, $\mathcal{H} = \mathcal{H}_A \otimes \mathcal{H}_B$, can experience a Type II QPT with a crossing of the two configurations. In this case, states with distinct properties coexist at similar energies, as shown schematically in Fig. 1(b). Usually, the individual Type I QPTs are masked by the strong mixing between the states in the separate configurations. However, if the mixing is weak, the abrupt Type II QPT is accompanied by a distinguished Type I QPT within each configuration separately. Such a scenario, referred to as intertwined QPTs [8–10], and its manifestation in Bose and Bose-Fermi systems is the subject matter of the present contribution.

2 Algebraic approach to quantum phase transitions in Bose systems

Algebraic models based on compact spectrum generating algebras are particularly useful for studying QPTs in mesoscopic (finite) systems. They are endowed with a rich symmetry structure, amenable for both quantum and classical analysis and provide a simple framework for tractable yet detailed calculation of observables. As a representative for this class of models in bosonic systems, we consider an interacting boson model for a single configuration and its extensions to multiple configurations.

2.1 The interacting boson model

The interacting boson model (IBM) [11], describes low-lying quadrupole collective states in even-even nuclei in terms of N interacting monopole (s) and quadrupole (d) bosons. The model is based on a $U(6)$ spectrum generating algebra with elements $\mathcal{G}_{ij} \equiv b_i^\dagger b_j = \{s^\dagger s, s^\dagger d_m, d_m^\dagger s, d_m^\dagger d_{m'}\}$. The IBM Hamiltonian is expanded in terms of these generators, $\hat{H} = \sum_{ij} \epsilon_{ij} \mathcal{G}_{ij} + \sum_{ijkl} u_{ijkl} \mathcal{G}_{ij} \mathcal{G}_{kl}$, and consists of Hermitian, rotational-invariant interactions which conserve the total number of s - and d -bosons, $\hat{N} = \hat{n}_s + \hat{n}_d = s^\dagger s + \sum_m d_m^\dagger d_m$. A dynamical symmetry (DS) occurs if the Hamiltonian can be written in terms of the Casimir operators of a chain of nested sub-algebras of $U(6)$. The Hamiltonian is then completely solvable in the basis associated with each chain. The solvable limits of the IBM correspond to the following DS chains,

$$U(6) \supset U(5) \supset SO(5) \supset SO(3) \quad |N, n_d, \tau, n_\Delta, L\rangle, \quad (4a)$$

$$U(6) \supset SU(3) \supset SO(3) \quad |N, (\lambda, \mu), K, L\rangle, \quad (4b)$$

$$U(6) \supset SO(6) \supset SO(5) \supset SO(3) \quad |N, \sigma, \tau, n_\Delta, L\rangle. \quad (4c)$$

The basis members indicated above, are classified by the irreducible representations (irreps) of the corresponding algebras. Specifically, the quantum numbers $N, n_d, (\lambda, \mu), \sigma, \tau, L$, label the relevant irreps of $U(6)$, $U(5)$, $SU(3)$, $SO(6)$, $SO(5)$, $SO(3)$, respectively, and n_Δ, K are multiplicity labels. The basis states are eigenstates of the DS Hamiltonian with energies expressed by the eigenvalues of the Casimir operators in a given chain.

In the $U(5)$ -DS limit, Eq. (4a), the spectrum resembles that of a spherical vibrator, where states are arranged in $U(5)$ n_d -multiplets at approximately equal energy spacing. The ground and lowest excited states are $(n_d=0, L=0)$ and $(n_d=1, L=2)$, $(n_d=2, L=0, 2, 4)$, $(n_d=3, L=2, 0, 3, 4, 6)$. The spectra in the $SU(3)$ -DS limit, Eq. (4b), resembles that of an axially-deformed prolate rotor with states arranged in $SU(3)$ (λ, μ) -multiplets forming rotational bands with $L(L+1)$ -splitting. The lowest irrep $(2N, 0)$ contains the ground band $g(K=0)$. The first excited irrep $(2N-4, 2)$ contains both the $\beta(K=0)$ and $\gamma(K=2)$ bands. The lowest members of each K -band have $L=0, 2, 4, \dots$ ($L=2, 3, 4, \dots$) for $K=0$ ($K=2$). The spectrum in the $SO(6)$ -DS limit of Eq. (4c), resembles that of a γ -unstable deformed rotor, where states are arranged in $SO(6)$ σ -multiplets forming rotational bands with $\tau(\tau+3)$ splitting. The lowest irrep $\sigma=N$ contains the ground (g) band and the first excited irrep $\sigma=N-2$ contains the β -band. The lowest members in each band have quantum numbers $(\tau=0, L=0)$, $(\tau=1, L=2)$, $(\tau=2, L=2, 4)$ and $(\tau=3, L=0, 3, 4, 6)$. Characteristic energy ratios for the $U(5)$, $SU(3)$, $SO(6)$ limits are $R_{4/2} = E(4_1)/E(2_1) = 2, 3.33, 2.5$, respectively.

Geometry is introduced in the algebraic model by means of a coset space $U(6)/U(5) \otimes U(1)$ and an energy surface,

$$E_N(\beta, \gamma) = \langle \beta, \gamma; N | \hat{H} | \beta, \gamma; N \rangle, \quad (5)$$

obtained by the expectation value of the Hamiltonian in a ‘projective’ coherent state [5, 12],

$$|\beta, \gamma; N\rangle = (N!)^{-1/2} (b_c^\dagger)^N |0\rangle, \quad (6a)$$

$$b_c^\dagger = (1 + \beta^2)^{-1/2} [\beta \cos \gamma d_0^\dagger + \beta \sin \gamma (d_2^\dagger + d_{-2}^\dagger) / \sqrt{2} + s^\dagger]. \quad (6b)$$

Here (β, γ) are quadrupole shape parameters whose values, $(\beta_{\text{eq}}, \gamma_{\text{eq}})$, at the global minimum of $E_N(\beta, \gamma)$ define the equilibrium shape for a given Hamiltonian. The equilibrium deformations associated with the DS limits, Eq. (4), conform with their geometric interpretation,

$$U(5) : \quad \beta_{\text{eq}} = 0 \quad \text{spherical shape}, \quad (7a)$$

$$SU(3) : \quad (\beta_{\text{eq}} = \sqrt{2}, \gamma_{\text{eq}} = 0) \quad \text{prolate-deformed shape}, \quad (7b)$$

$$SO(6) : \quad (\beta_{\text{eq}} = 1, \gamma_{\text{eq}} \text{ arbitrary}) \quad \gamma\text{-unstable deformed shape}. \quad (7c)$$

The coherent state $|\beta_{\text{eq}}, \gamma_{\text{eq}}; N\rangle$ of Eq. (6), with the equilibrium deformations, serves as an intrinsic state for the ground band, whose rotational members are obtained by angular momentum projection.

2.2 Microscopic consideration

A microscopic interpretation of the IBM is based on its link with the nuclear shell model [13]. According to it, the s and d bosons represent valence nucleon pairs with total number $N = N_\pi + N_\nu$, where N_π (N_ν) is the number of proton (neutron) particle or hole pairs counted from the nearest closed shell. The states constructed of valence nucleons are referred to as normal states. The Type I QPTs discussed in Section 2.3. are structural changes involving a subset of normal states represented by a single configuration of N bosons. In nuclei near closed shells, additional configurations associated with particle-hole excitations across shell gaps, play a role. The resulting states are referred to as intruder states [6]. The latter can drop in energy and coexist with normal states due to correlations induced by the residual interactions [14, 15]. Type II QPTs involving the crossing of normal and intruder states, can be modeled in the IBM by incorporating additional configurations with different boson numbers, in the manner described in Section 2.4.

2.3 Type I QPT

In the algebraic approach to QPTs, the dynamical symmetries correspond to possible shape-phases of the system in accord with their geometric interpretation. QPTs in a single configuration (Type I) can be studied by an Hamiltonian $\hat{H}(\xi)$, as in Eq. (1), which interpolates between the different DS limits (phases) by varying the control parameter ξ [5, 16]. The energy surface, $E_N(\xi; \beta, \gamma)$ of Eq. (5), depends parametrically on ξ and serves as the classical mean-field Landau potential. The nature of the phase transition and critical points are determined by the derivatives with respect to ξ of the energy surface, evaluated at the equilibrium deformations. The order of the QPT is the order of the derivative where discontinuities first occur (Ehrenfest classification) [2].

A typical Hamiltonian frequently used for Type I QPTs has the form,

$$\hat{H}(\epsilon_d, \kappa, \chi) = \epsilon_d \hat{n}_d + \kappa \hat{Q}_\chi \cdot \hat{Q}_\chi, \quad (8)$$

where the quadrupole operator is given by,

$$\hat{Q}_\chi = d^\dagger s + s^\dagger \tilde{d} + \chi (d^\dagger \times \tilde{d})^{(2)}. \quad (9)$$

Here $\tilde{d}_m = (-1)^m d_{-m}$ and standard notation of angular momentum coupling is used. The control parameters $(\epsilon_d, \kappa, \chi)$ in Eq. (8) with values $(\kappa=0)$, $(\epsilon_d=0, \chi=-\sqrt{7}/2)$ and $(\epsilon_d=0, \chi=0)$, interpolate between the respective U(5), SU(3) and SO(6) DS limits. For the Hamiltonian (8), the associated Landau potential (5) reads,

$$E_N(\beta, \gamma; \epsilon_d, \kappa, \chi) = 5\kappa N + \frac{N\beta^2}{1+\beta^2} [\epsilon_d + \kappa(\chi^2 - 4)] + \frac{N(N-1)\beta^2}{(1+\beta^2)^2} \kappa [4 - 4\bar{\chi}\beta \cos 3\gamma + \bar{\chi}^2\beta^2], \quad (10)$$

where $\bar{\chi} = \sqrt{\frac{2}{7}}\chi$. The U(5)-SU(3) transition is found to be first-order, the U(5)-SO(6) transition is second order and the SU(3)-SO(6) transition is a crossover. The order parameter is taken to be the expectation value of the d -boson number operator, \hat{n}_d , in the ground state. The latter converges in the large- N limit to the classical order parameter related to the equilibrium deformation β_{eq} ,

$$\frac{\langle \hat{n}_d \rangle_{0_1^+}}{N} \approx \frac{\beta_{\text{eq}}^2}{1 + \beta_{\text{eq}}^2}. \quad (11)$$

IBM Hamiltonians of the above form have been used extensively for studying shape-phase transitions, exemplifying Type I QPTs in nuclei [4, 16–19].

2.4 Type II QPT

The effect of additional configurations, representing intruder states in nuclei, can be studied in the framework of the interacting boson model with configuration mixing (IBM-CM) [20, 21]. The latter is an extension of the IBM based on associating the different shell-model spaces of 0p-0h, 2p-2h, 4p-4h, . . . particle-hole excitations, with the corresponding boson spaces comprising of N , $N+2$, $N+4$, . . . bosons,

which are subsequently mixed. For two configurations, the IBM-CM Hamiltonian has the form as in Eq. (2) with entries,

$$\hat{H}_A(\xi_A) = \hat{H}(\epsilon_d^A, \kappa_A, \chi), \quad (12a)$$

$$\hat{H}_B(\xi_B) = \hat{H}(\epsilon_d^B, \kappa_B, \chi) + \kappa'_B \hat{L} \cdot \hat{L} + \Delta, \quad (12b)$$

$$\hat{W}(\omega) = \omega [(d^\dagger \times d^\dagger)^{(0)} + (s^\dagger)^2] + \text{H.c.}, \quad (12c)$$

where H.c. stands for Hermitian conjugate. The Hamiltonian \hat{H}_A represents the normal A configuration (N boson space) and \hat{H}_B represents the intruder B configuration ($N+2$ boson space). They involve terms similar to those of the single-configuration Hamiltonian of Eq. (8). \hat{H}_B contains an additional rotational term and an off-set Δ between the two configurations. The resulting eigenstates $|\Psi; L\rangle$ are linear combinations of the wave functions, Ψ_A and Ψ_B , in the two spaces $[N]$ and $[N+2]$,

$$|\Psi; L\rangle = a|\Psi_A; [N], L\rangle + b|\Psi_B; [N+2], L\rangle, \quad a^2 + b^2 = 1. \quad (13)$$

The normal and intruder components of $|\Psi; L\rangle$ can be expanded in the any of the DS bases of Eq. (4) with the appropriate boson numbers,

$$|\Psi; L\rangle = \sum_{\alpha} C_{\alpha}^{(N,L)} |N, \alpha, L\rangle + \sum_{\alpha} C_{\alpha}^{(N+2,L)} |N+2, \alpha, L\rangle, \quad (14)$$

where α denotes (n_d, τ, n_{Δ}) , $[(\lambda, \mu), K]$ and $(\sigma, \tau, n_{\Delta})$ for the U(5), SU(3) and SO(6) chains, respectively. From such expansions one can extract the probabilities for a given symmetry species,

$$\text{U(5)}: P_{n_d}^{(N,L)} = \sum_{\tau, n_{\Delta}} [C_{n_d, \tau, n_{\Delta}}^{(N,L)}]^2, \quad P_{n_d}^{(N+2,L)} = \sum_{\tau, n_{\Delta}} [C_{n_d, \tau, n_{\Delta}}^{(N+2,L)}]^2, \quad (15a)$$

$$\text{SU(3)}: P_{(\lambda, \mu)}^{(N,L)} = \sum_K [C_{(\lambda, \mu), K}^{(N,L)}]^2, \quad P_{(\lambda, \mu)}^{(N+2,L)} = \sum_K [C_{(\lambda, \mu), K}^{(N+2,L)}]^2, \quad (15b)$$

$$\text{SO(6)}: P_{\sigma}^{(N,L)} = \sum_{\tau, n_{\Delta}} [C_{\sigma, \tau, n_{\Delta}}^{(N,L)}]^2, \quad P_{\sigma}^{(N+2,L)} = \sum_{\tau, n_{\Delta}} [C_{\sigma, \tau, n_{\Delta}}^{(N+2,L)}]^2. \quad (15c)$$

The above DS decompositions highlight the symmetry and shape content, Eq. (7), of the states considered. In particular, spherical-type of states are dominated by a single n_d component in the U(5) probabilities, Eq. (15a), while deformed type of states show a large spread in n_d . The probabilities of the normal-intruder mixing for the state $|\Psi; L\rangle$, Eqs. (13)-(14), are given by,

$$a^2 = \sum_{\alpha} |C_{\alpha}^{(N,L)}|^2, \quad b^2 = \sum_{\alpha} |C_{\alpha}^{(N+2,L)}|^2 = 1 - a^2. \quad (16)$$

The $E2$ operator in the IBM-CM reads $\hat{T}(E2) = e_A \hat{Q}_{\chi}^{(N)} + e_B \hat{Q}_{\chi}^{(N+2)}$, where \hat{Q}_{χ} is defined in Eq. (9), a superscript (N) denotes a projection onto the $[N]$ boson space and (e_A, e_B) are boson effective charges.

A geometric interpretation [22] is obtained by means of the matrix $E(\beta, \gamma)$,

$$E(\beta, \gamma) = \begin{bmatrix} E_A(\beta, \gamma; \xi_A) & \Omega(\beta, \gamma; \omega) \\ \Omega(\beta, \gamma; \omega) & E_B(\beta, \gamma; \xi_B) \end{bmatrix}, \quad (17)$$

whose entries are the matrix elements of the corresponding terms in the Hamiltonian (2), between the intrinsic states (6) of the two configurations, with appropriate boson numbers. The explicit expressions are found to be,

$$E_A(\beta, \gamma; \xi_A) = E_N(\beta, \gamma; \epsilon_d^A, \kappa_A, \chi), \quad (18a)$$

$$E_B(\beta, \gamma; \xi_B) = E_{N+2}(\beta, \gamma; \epsilon_d^B, \kappa_B, \chi) + 6\kappa'_B \frac{(N+2)\beta^2}{1+\beta^2} + \Delta, \quad (18b)$$

$$\Omega(\beta, \gamma; \omega) = \frac{\sqrt{(N+2)(N+1)}}{1+\beta^2} \omega \left(1 + \frac{1}{\sqrt{5}} \beta^2 \right), \quad (18c)$$

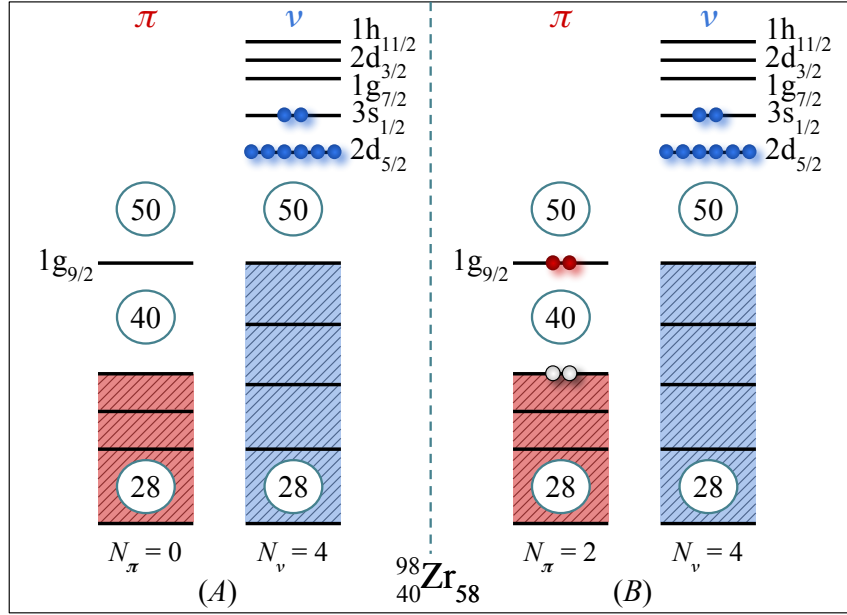


Figure 2: Schematic representation of the two shell-model configurations (A and B) for ${}^{98}_{40}\text{Zr}_{58}$. The corresponding numbers of proton bosons (N_π) and neutron bosons (N_ν) are listed for each configuration and $N = N_\pi + N_\nu$.

where the surfaces on the right-hand-side of Eqs. (18a)-(18b) are obtained from Eq. (10).

Diagonalization of this two-by-two matrix produces the so-called eigen-potentials, $E_\pm(\beta, \gamma)$.

$E(\beta, \gamma)$ of Eq. (17) depends on the Hamiltonian's parameters (ξ_A, ξ_B, ω) and in Type II QPTs, serves as the Landau potential matrix [7]. The order parameters are taken to be the expectation value of \hat{n}_d in the ground state wave function, $|\Psi; L = 0_1^+\rangle$, and in its Ψ_A and Ψ_B components (13), denoted by $\langle \hat{n}_d \rangle_{0_1^+}$, $\langle \hat{n}_d \rangle_A$ and $\langle \hat{n}_d \rangle_B$, respectively. As can be inferred from Eq. (11), $\langle \hat{n}_d \rangle_A$ and $\langle \hat{n}_d \rangle_B$ provide information on the shape of each configuration, A and B. $\langle \hat{n}_d \rangle_{0_1^+}$ involves their sum weighted by the probabilities of each component,

$$\langle \hat{n}_d \rangle_{0_1^+} = a^2 \langle \hat{n}_d \rangle_A + b^2 \langle \hat{n}_d \rangle_B, \quad (19)$$

and portrays the effect of the normal-intruder mixing on the shape of the ground state.

IBM-CM Hamiltonians and surfaces of the above form have been used extensively for studying shape-coexistence and crossing of different configurations, exemplifying Type II QPTs in nuclei near (sub-) shell closure [8–10, 20–27].

2.5 IBM-CM in the Zirconium chain of isotopes

The IBM-CM framework has been used in [8–10] to calculate spectral properties of low-lying states in ${}^{92-110}\text{Zr}$. In a shell model approach, ${}^{90}\text{Zr}$ is taken as a core and valence neutrons in the 50–82 major shell. The normal A configuration corresponds to having no active protons above $Z=40$ sub-shell gap and the intruder B configuration corresponds to two-proton excitation from below to above this gap, creating 2p-2h states. In the algebraic approach, the model space consists of $[N] \oplus [N+2]$ boson spaces. Here $N = N_\pi + N_\nu$ with $N_\pi=0$ ($N_\pi=2$) proton bosons for the A (B) configuration and N_ν neutron bosons whose number is determined by the usual boson-counting. The two configurations relevant for ${}^{98}\text{Zr}$ are shown schematically in Fig. 2. For a given isotope and choice of model space, the parameters of the Hamiltonian and transition operator are determined by a fit to the spectra and $E2$ transitions in a manner described in Ref. [10]. Apart from some fluctuations due to the subshell closure at neutron number 56 (the filling of the $\nu 2d_{5/2}$ orbital), the values of the parameters, shown in Fig. 3 and Table V of [10], are a smooth function of neutron number and, in some cases, a constant. A notable exception is the sharp decrease by 1 MeV of the energy off-set parameter Δ (12b) beyond neutron number 56, reflecting the effects of the proton-neutron residual interaction [14, 15]. The parameter ω of the mixing term (12c), is constant except for ${}^{92,94}\text{Zr}$ where the normal configuration space is small ($N=1, 2$).

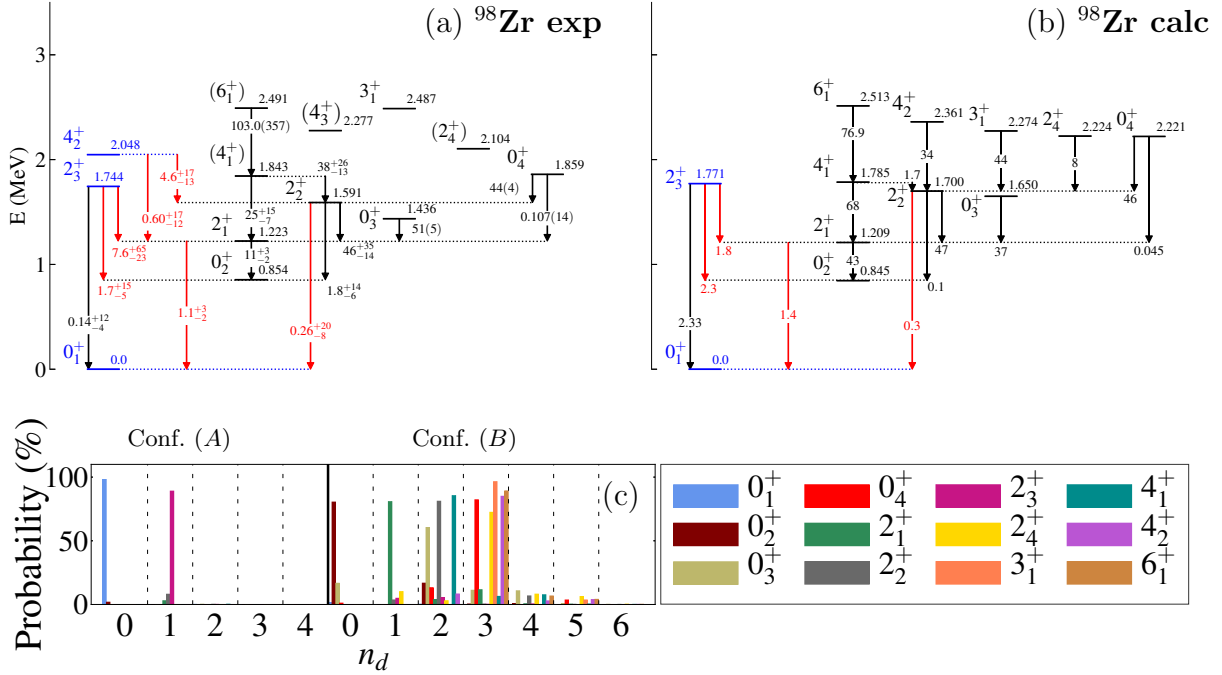


Figure 3: (a) Experimental and (b) calculated energy levels in MeV and $E2$ transition rates in Weisskopf units (W.u.) for ^{98}Zr . (c) U(5) n_d -decomposition, Eq. (15a), for eigenstates of the IBM-CM Hamiltonian, Eq. (12), assigned to the normal (A) and intruder (B) configurations. Adapted from [10].

As an example of the quantum analysis for individual nuclei, we present in Fig. 3 the experimental and calculated spectra and $E2$ rates for low-lying states in ^{98}Zr and their U(5) n_d -decomposition. The assignment of states as normal or intruder is based on their measured $E2$ decays when available, or on their calculated probabilities, a^2 and b^2 , of Eq. (16). The 0_1^+ , and 2_3^+ states are assigned to the normal A configuration. As shown in Fig 3(c), the n_d -probability of their normal part, $P_{nd}^{(N,L)}$ of Eq. (15a), exhibits a single dominant n_d -component ($n_d \approx 0, 1$), respectively, which identifies them as spherical type of states. The remaining states in Fig. 3(b) are assigned to the intruder B configuration and exhibit a spectra of perturbed n_d multiplets. The n_d -probability of their intruder part, $P_{nd}^{(N+2,L)}$ of Eq. (15a), shows a slightly reduced dominance of single components with $n_d \approx 0, 1, 2, 3$ and a small spread in n_d . These observations suggest that these states are quasi-spherical or weakly deformed, an interpretation supported by the measured $E2$ rates.

A similar analysis can be done for all $^{92-110}\text{Zr}$ isotopes. In Fig. 4 we show a comparison between experimental and calculated levels along with assignments to configurations and to the closest dynamical symmetry for each state. In the region between neutron number 50 and 56, one observes two weakly coupled structures: a spherical A configuration (seniority-like) and a weakly deformed B configuration, as evidenced by the ratio $R_{4/2}^{(A)} \cong 1.6$ and $R_{4/2}^{(B)} \cong 2.3$. From neutron number 58, there is a pronounced drop in energy for the states of the B configuration and at 60, the two configurations exchange their role, indicating a Type II QPT. At this stage, the intruder B configuration appears to be at the critical point of a U(5)-SU(3) Type I QPT, as evidenced by the low value of the energy of the first excited 0^+ state of this configuration. Beyond neutron number 60, the intruder B configuration is strongly deformed, as evidenced by the small value of $E(2_2^+)$ and by the ratio $R_{4/2}^{(B)} = 3.24$ in ^{104}Zr . At still larger neutron number 66, the ground state band becomes γ -unstable, as evidenced by the close energy of the states 2_2^+ and 4_1^+ in ^{106}Zr and ^{110}Zr , a signature of the SO(6) symmetry. In this region, the ground (B) configuration shows spectral features of a crossover from SU(3) to SO(6).

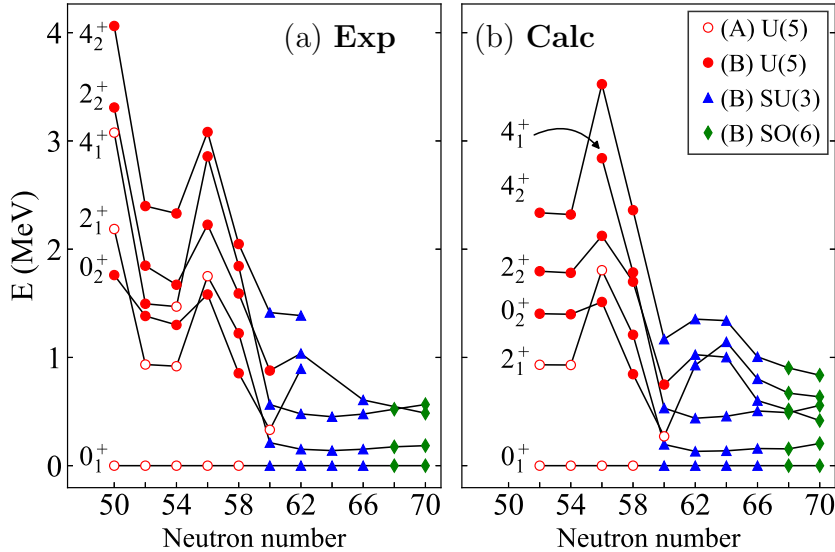


Figure 4: Comparison between (a) experimental and (b) calculated energy levels 0_1^+ , 2_1^+ , 4_1^+ , 0_2^+ , 2_2^+ , 4_2^+ in the Zr isotopes. Empty (filled) symbols indicate a state dominated by the normal A configuration (intruder B configuration), with assignments based on Eq. (16). The shape of the symbol [\circ , \triangle , \diamond], indicates the closest dynamical symmetry [U(5), SU(3), SO(6)] to the state considered, based on Eq. (15). Adapted from [8].

2.6 Intertwined QPTs in the Zr chain

The above spectral analysis suggests a situation of coexisting Type I and Type II QPTs, which is the defining property of intertwined QPTs. In order to understand the nature of these phase transitions, it is instructive to examine the behavior of the order parameters, the configuration content and symmetry properties of the evolving states.

Fig. 5(a) shows the evolution with neutron number of the order parameters, $\langle \hat{n}_d \rangle_{0_1^+}$, $\langle \hat{n}_d \rangle_A$, $\langle \hat{n}_d \rangle_B$, Eq. (19), of the ground state wave function, $|\Psi; L=0_1^+\rangle$ and its Ψ_A , Ψ_B components, normalized by the respective boson numbers: $\langle \hat{N} \rangle_{0_1^+} = a^2 N + b^2(N+2)$, $\langle \hat{N} \rangle_A = N$, $\langle \hat{N} \rangle_B = N+2$. The A configuration is seen to be spherical for all neutron numbers considered. In contrast, the B configuration is weakly-deformed for neutron number 52-58. One can see here clearly a jump between 58 and 60 from the A - to the B configuration, indicating a Type II QPT, a further increase at 60-64, indicating a U(5)-SU(3) Type I QPT and, finally, there is a decrease at 66, indicating a crossover from SU(3) to SO(6). $\langle \hat{n}_d \rangle_{0_1^+}$ is close to $\langle \hat{n}_d \rangle_A$ for 52-58 and coincides with $\langle \hat{n}_d \rangle_B$ at 60 and above, consistent with a high degree of purity with respect to configuration-mixing.

Fig. 5(b) shows the probability b^2 of the Ψ_B component, Eq. (16), in the wave functions of the ground state (0_1^+) and first-excited state (2_1^+). The rapid change in structure of 0_1^+ from the normal A configuration in $^{92-98}\text{Zr}$ (small b^2) to the intruder B configuration in $^{100-110}\text{Zr}$ (large b^2) is clearly evident, signaling a Type II QPT. The configuration change appears sooner in 2_1^+ , which changes to the B configuration already in ^{98}Zr . Outside a narrow region near neutron number 60, where the crossing occurs, the two configurations are weakly mixed and the states retain a high level of purity.

The shape-evolution within the B configuration is reflected in the change of symmetries in the lowest 0_B^+ state of this configuration. As shown in Fig. 5(c), the probability of the U(5) irrep $n_d = 0$, Eq. (15a), is large ($\sim 90\%$) for neutron number 52-58, indicating a spherical type of state. At 60 and beyond, it drops drastically, indicating appreciable n_d -mixing and a transition to a deformed state. This behavior is consistent with the observed rise in probability of the SU(3) irrep $(\lambda, \mu) = (2N+4, 0)$, Eq. (15b), for neutron number 60-64, signaling a U(5)-SU(3) Type I QPT. From 66 and beyond one sees a dominant probability of the SO(6) irrep $\sigma = N+2$, Eq. (15c), suggesting a crossover from SU(3) to SO(6). A very similar trend is observed for the 2_B^+ state. The findings of Fig. 5 support the claim for the occurrence of two configurations in Zr isotopes that are weakly mixed and interchange their roles in the ground state while their individual shapes evolve gradually with neutron number, *i.e.* intertwined Type I and II QPTs.

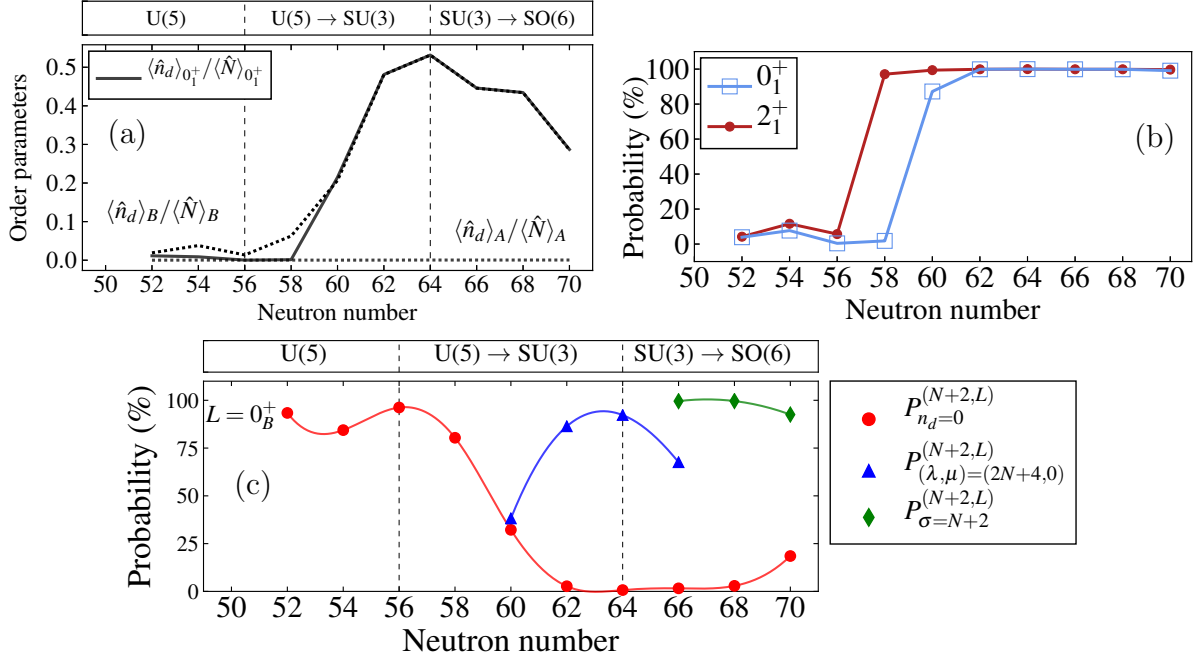


Figure 5: Evolution of structure along the Zr chain. (a) Order parameters: $\langle \hat{n}_d \rangle_{0_1^+}$ (solid line) and $\langle \hat{n}_d \rangle_A$, $\langle \hat{n}_d \rangle_B$ (dotted lines), defined in Section 2.4, normalized by the respective boson numbers. (b) Percentage of the wave functions within the intruder B configuration [the b^2 probability of Eq. (16)], for the ground (0_1^+) and excited (2_1^+) states. (c) Symmetry properties of the lowest 0_B^+ state in the intruder B configuration. Shown are the probabilities of selected U(5) (●), SU(3) (◆), and SO(6) (▲) irreps in 0_B^+ , obtained from Eq. (15).

2.7 Evolution of observables along the Zr chain

The above conclusions are stressed by an analysis of other observables. In particular, the $B(E2)$ values for $2^+ \rightarrow 0^+$ transitions, shown in Fig. 6(a), follow the same trends as the respective order parameters, seen in Fig. 5(a). The isotope shift $\Delta \langle \hat{r}^2 \rangle_{0_1^+}$, shown in Fig. 6(b), increases at the transition point and decreases afterwards, in accord with the expected behaviour of a first-order Type I QPT. (In the large N limit, this quantity, proportional to the derivative of the order parameter $\langle \hat{n}_d \rangle_{0_1^+}$, diverges at the critical-point). The two-neutron separation energy S_{2n} , shown in Fig. 6(c), is a straight line for neutron number 52-56, as the ground state is spherical (seniority-like) A configuration. After 56, it first goes down due to the subshell closure at 56, then it flattens as expected from a first-order Type I QPT. After 62, it goes down again due to the increase of deformation and finally it flattens as expected from a crossover from SU(3) to SO(6). Lastly, the magnetic moments of the 2_1^+ states in Zr isotopes, shown in Fig. 6(d), exhibit a jump from small (or negative) single-particle values for neutron numbers 52-56, to large collective (rigid rotor) values for 58-70.

2.8 Classical analysis

One of the main advantages of the algebraic approach is that one can do both a quantum and a classical analysis. In Fig. 7, we show the calculated lowest eigen-potential $E_-(\beta, \gamma)$, obtained by diagonalizing the matrix of Eq. (17). These classical potentials confirm the quantum results, as they show a transition from spherical ($^{92-98}\text{Zr}$), to a flat-bottomed potential at ^{100}Zr , to prolate axially-deformed ($^{102-104}\text{Zr}$), and finally to γ -unstable ($^{106-110}\text{Zr}$).

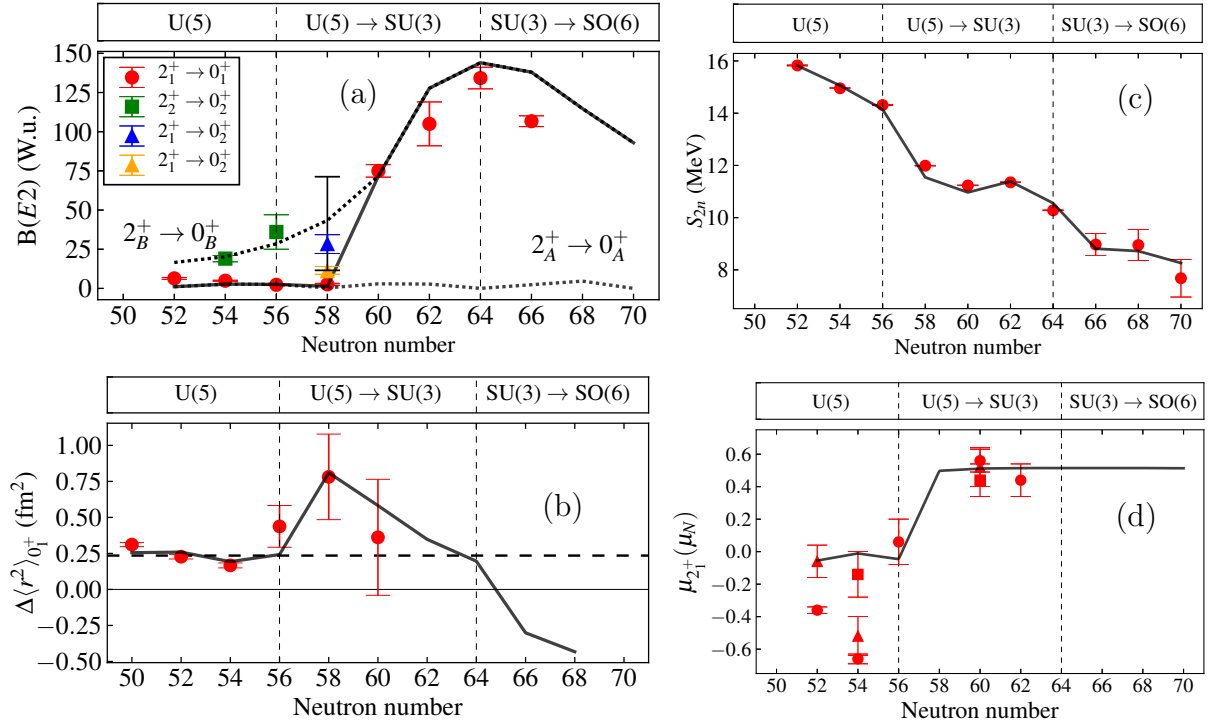


Figure 6: Evolution of observables along the Zr chain. Symbols (solid lines) denote experimental data (calculated results). (a) $B(E2; 2^+ \rightarrow 0^+)$ in W.u. (b) Isotope shift $\Delta \langle \hat{r}^2 \rangle_{0_1^+}$ in fm^2 . (c) Two-neutron separation energies S_{2n} in MeV. (d) Magnetic moments $\mu_{2_1^+}$ in units of nuclear magneton (μ_N).

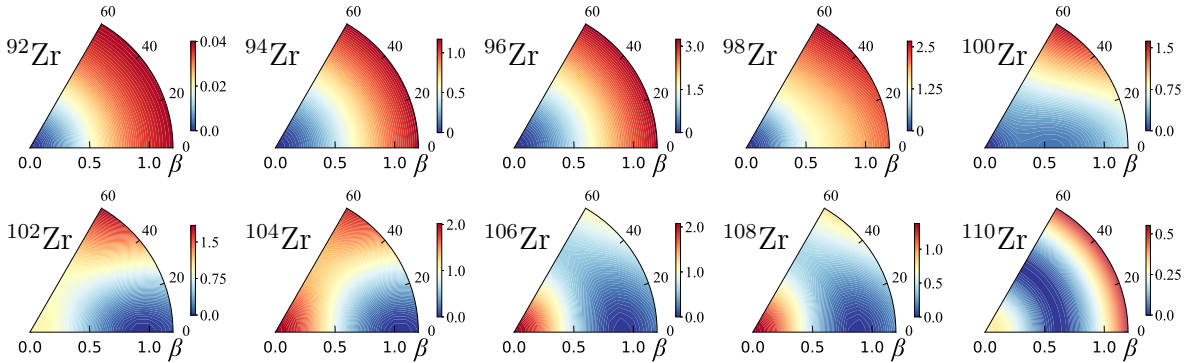


Figure 7: Contour plots in the (β, γ) plane of the lowest eigen-potential surface, $E_-(\beta, \gamma)$ mentioned in Section 2.4, for the $^{92-110}\text{Zr}$ isotopes. β is a radial coordinate and the angle γ is in degrees. Adapted from [8].

3 Algebraic approach to quantum phase transitions in Bose-Fermi systems

The study of QPTs in a Bose-Fermi system is more complex due to the presence of both collective (bosonic) and single-particle (fermionic) degrees of freedom with different statistics. As a representative for the algebraic approach to such systems, we consider the interacting boson-fermion model (IBFM) [28], a model of odd-even nuclei phrased in terms of correlated pairs with $L = 0, 2$ (s, d bosons) and unpaired particles with angular momentum j (j fermions). The model is based on a $U_b(6) \otimes U_f(\Omega)$ spectrum generating algebra, where $U_b(6)$ is the bosonic algebra of the IBM discussed in Section 2.1 and $U_f(\Omega)$ is the fermion algebra with Ω the dimension of the single-fermion space. Here we focus the discussion to the case of a single- j fermion for which $\Omega = 2j + 1$.

The IBFM Hamiltonian contains boson- fermion- and boson-fermion parts,

$$\hat{H} = \hat{H}_b + \hat{H}_f + \hat{V}_{bf} , \quad (20)$$

where,

$$\hat{H}_b(\epsilon_d, \kappa, \chi) = \epsilon_d \hat{n}_d + \kappa \hat{Q}_\chi \cdot \hat{Q}_\chi , \quad (21a)$$

$$\hat{H}_f(\epsilon_j) = \epsilon_j \hat{n}_j , \quad (21b)$$

$$\hat{V}_{bf}(A, \Gamma, \Lambda) = V_{bf}^{\text{MON}} + \hat{V}_{bf}^{\text{QUAD}} + \hat{V}_{bf}^{\text{EXC}} . \quad (21c)$$

\hat{H}_b is the IBM Hamiltonian, taken to be as in Eq. (8), describing the dynamics of the even-even core. \hat{H}_f involves the fermion number operator $\hat{n}_j = \sum_m a_{j,m}^\dagger a_{j,m}$ and \hat{V}_{bf} is composed of monopole, quadrupole and exchange terms given by,

$$V_{bf}^{\text{MON}} = A \hat{n}_d \hat{n}_j , \quad (22a)$$

$$\hat{V}_{bf}^{\text{QUAD}} = \Gamma \hat{Q}_\chi \cdot (a_j^\dagger \times \tilde{a}_j)^{(2)} , \quad (22b)$$

$$\hat{V}_{bf}^{\text{EXC}} = \Lambda \sqrt{2j+1} : [(d^\dagger \tilde{a}_j)^{(j)} \times (\tilde{d} a_j^\dagger)^{(j)}]^{(0)} : , \quad (22c)$$

where $\tilde{a}_{j,m} = (-1)^{j-m} a_{j,-m}$ and $::$ denotes normal ordering.

3.1 Type I QPT

In Type I QPTs, the coupling constants of the IBFM Hamiltonian, Eqs. (20)-(22), serve as control parameters. As discussed in Section 2.3, the boson part $\hat{H}_b(\epsilon_d, \kappa, \chi)$ interpolates between the DS limits of the IBM and describes a shape-phase transition in the even-even core. The boson-fermion terms in $\hat{V}_{bf}(A, \Gamma, \Delta)$ control the coupling of the odd fermion to the boson core. IBFM Hamiltonians of the above form have been widely used to study Type I QPTs in odd-even nuclei [28–33].

For studying the effect of the fermion on QPTs in bosonic systems and interpreting the structural changes taking place, it is instructive to consider known coupling schemes of the odd fermion to different core shapes. If the shape of the core is spherical, the weak coupling scheme is appropriate, where the wave functions are written as,

$$|\Psi; [N], L, j; J\rangle = |N, n_d, \tau, n_\Delta, (L \otimes j) J\rangle \quad J = |L - j|, |L - j| + 1, \dots, (L + j) . \quad (23)$$

Here U(5) basis states $|N, n_d, \tau, n_\Delta, L\rangle$, Eq. (4a), are coupled to the fermion state $|j\rangle$, to form a multiplet of states with total angular momentum J in the range of values specified above.

If the core has an axially-deformed prolate shape, the strong coupling scheme is appropriate, with wave functions of the form,

$$|\Psi; [N], j, K; J\rangle = \sqrt{\frac{2}{2J+1}} \sum_{L=0,2,4,\dots} \sqrt{2L+1} (L, 0; j, K | J, K) |N, (2N, 0), K_b = 0, (L \otimes j) J\rangle , \quad (24)$$

where $J = K, K + 1, K + 2, \dots$ and $(|)$ stands for a Clebsch Gordan coefficient. Here states of the SU(3) ground band $|N, (2N, 0), K_b = 0, L\rangle$, Eq. (4b) with $L \geq 0$ even, are coupled to the angular momentum j of the odd fermion to form rotational K -bands with angular momentum projection $K = j, j - 1, \dots, 1/2$, along the symmetry axis. The relative order of different K -bands is governed by the strengths Γ and Λ of the quadrupole and exchange terms [34]. For a general prolate-deformed shape, away from the SU(3) limit, the relevant strong-coupling wave functions are obtained by replacing in Eq. (24) the SU(3) basis states by the L -states projected from the intrinsic state $|\beta_{\text{eq}}, \gamma_{\text{eq}} = 0; N\rangle$, Eq. (6), with the equilibrium deformations.

3.2 Type II QPT

To allow for core excitations and accommodate several configurations, the IBFM can be extended to obtain the interacting boson-fermion model with configuration mixing (IBFM-CM) [35,36]. The Hamiltonian is composed of boson-, fermion- and boson-fermion parts, which now become matrices. For two configurations (A, B) it has the form $\hat{H} = \hat{H}_b + \hat{H}_f + \hat{V}_{bf}$ with,

$$\hat{H}_b = \begin{bmatrix} \hat{H}_b^A(\xi_A) & \hat{W}_b(\omega) \\ \hat{W}_b(\omega) & \hat{H}_b^B(\xi_B) \end{bmatrix} , \quad \hat{H}_f = \begin{bmatrix} \epsilon_j^A \hat{n}_j & 0 \\ 0 & \epsilon_j^B \hat{n}_j \end{bmatrix} , \quad \hat{V}_{bf} = \begin{bmatrix} \hat{V}_{bf}^A(\zeta_A) & \hat{W}_{bf}(\omega_j) \\ \hat{W}_{bf}(\omega_j) & \hat{V}_{bf}^B(\zeta_B) \end{bmatrix} . \quad (25)$$

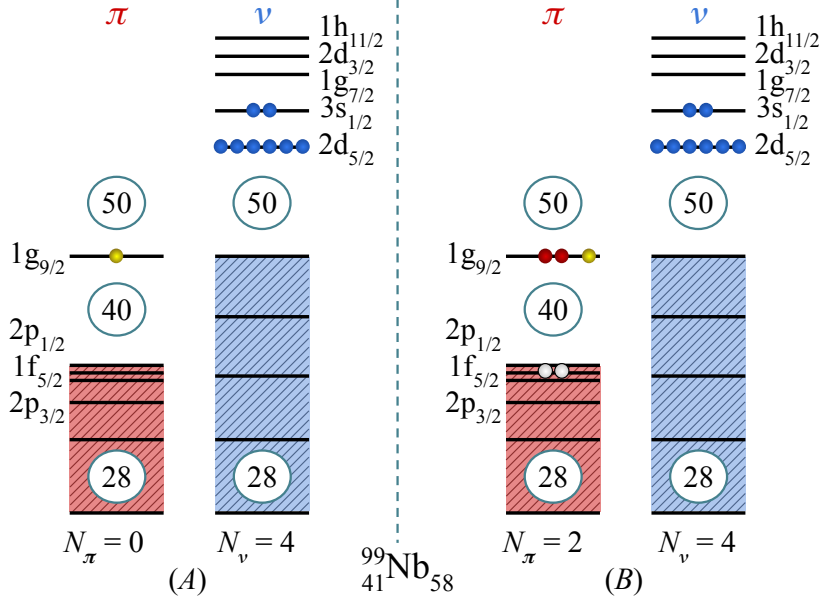


Figure 8: Schematic representation of the two shell-model configurations (A and B) for ${}^{99}_{41}\text{Nb}_{58}$. The corresponding numbers of proton bosons (N_π) and neutron bosons (N_ν), are listed for each configuration and $N = N_\pi + N_\nu$.

\hat{H}_b coincides with the IBM-CM Hamiltonian, discussed in Section 2.4, with entries given in Eq. (12). It acts in the boson spaces $[N] \oplus [N+2]$, representing the normal (A) and intruder (B) configurations. \hat{H}_f involves the one-body fermion number operator for each configuration. \hat{V}_{bf} involves monopole, quadrupole and exchange two-body terms, Eq. (22), for each configuration and a mixing term,

$$\hat{W}_{bf} = \omega_j \hat{n}_j [(d^\dagger d^\dagger)^{(0)} + (s^\dagger)^2 + \text{H.c.}] . \quad (26)$$

For simplicity, the parameters of \hat{H}_f and \hat{V}_{bf} are taken to be the same in both configurations, *i.e.*, $\epsilon_j^A = \epsilon_j^B = \epsilon_j$ and $\zeta_A = \zeta_B = (A, \Gamma, \Lambda)$, and $\omega_j = 0$ since \hat{W}_{bf} coincides with \hat{W}_b for a single- j fermion.

The eigenstates $|\Psi; j, J\rangle$ of the IBFM-CM Hamiltonian, Eq. (25), are linear combinations of wave functions Ψ_A and Ψ_B , involving bosonic basis states in the two spaces $[[N], \alpha, L]$ and $[[N+2], \alpha, L]$, coupled to a j -fermion. Here α denotes additional quantum numbers of the dynamical symmetry chain, Eq. (4). The boson (L) and fermion (j) angular momenta are coupled to J ,

$$\begin{aligned} |\Psi; j, J\rangle &= a|\Psi_A, [N], j; J\rangle + b|\Psi_B, [N+2], j; J\rangle \\ &= \sum_{\alpha, L} C_{\alpha, L, j}^{(N, J)} |N, \alpha, (L \otimes j)J\rangle + \sum_{\alpha, L} C_{\alpha, L, j}^{(N+2, J)} |N+2, \alpha, (L \otimes j)J\rangle . \end{aligned} \quad (27)$$

The probability of normal-intruder mixing is given by,

$$a^2 = \sum_{\alpha, L} |C_{\alpha, L, j}^{(N, J)}|^2 \quad , \quad b^2 = \sum_{\alpha, L} |C_{\alpha, L, j}^{(N+2, J)}|^2 = 1 - a^2 . \quad (28)$$

Operators inducing electromagnetic transitions contain boson and fermion parts, *e.g.*, the $E2$ operator has the form $\hat{T}(E2) = e_A \hat{Q}_\chi^{(N)} + e_B \hat{Q}_\chi^{(N+2)} + e_f (a_j^\dagger \times \tilde{a}_j)^{(2)}$, with effective charges (e_A, e_B, e_f).

3.3 IBFM-CM in the Niobium chain of isotopes

The IBFM-CM framework has been applied in [35, 36] to calculate spectral properties of low-lying states in the ${}^A_{41}\text{Nb}$ isotopes with mass number $A=93-105$. In a shell model approach, these isotopes are described by coupling a proton to their respective ${}_{40}\text{Zr}$ cores with neutron number 52–64. The latter

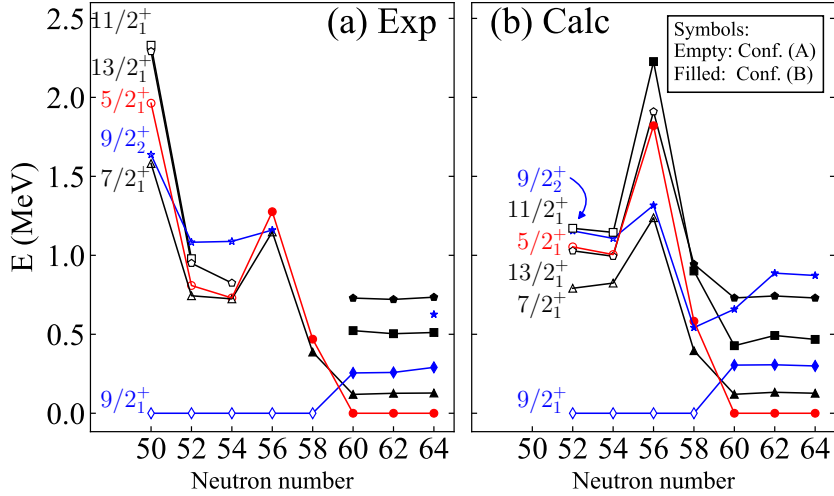


Figure 9: Comparison between (a) experimental and (b) calculated lowest-energy positive-parity levels in Nb isotopes. Empty (filled) symbols indicate a state dominated by the normal A configuration (intruder B configuration), with assignments based on Eq. (28). In particular, the $9/2_1^+$ state is in the A (B) configuration for neutron number 52–58 (60–64) and the $5/2_1^+$ state is in the A (B) configuration for 52–54 (56–64). Adapted from [35].

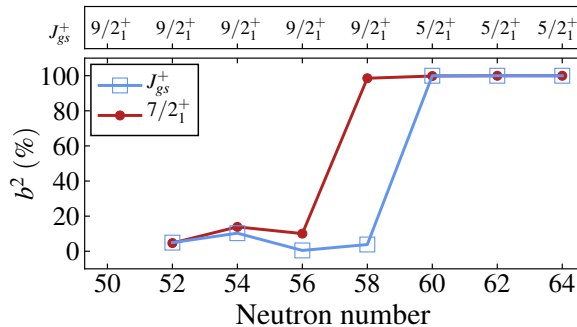


Figure 10: Percentage of the intruder (B) component [the b^2 probability of Eq. (28)], in the ground state (J_{gs}^+) and first-excited positive-parity state ($7/2_1^+$) of $^{93-103}\text{Nb}$. The values of J_{gs}^+ are indicated at the top.

involve the normal (A) and intruder (B) configurations, as outlined in Section 2.5. In the present contribution, we focus on the positive-parity states in the Nb isotopes (negative parity states are addressed in [36]). Such a case reduces to a single- j calculation where the IBFM-CM model space consists of a proton in a $\pi(1g_{9/2})$ orbit plus $[N] \oplus [N+2]$ boson spaces. The two configurations relevant for ^{99}Nb are shown schematically in Fig. 8. The parameters of the IBFM-CM Hamiltonian and transition operators are determined from a fit in the manner described in [35, 36]. The parameters of the boson part \hat{H}_b are taken to be the same as in the Zr calculation [10]. The Bose-Fermi couplings in $\hat{V}_{\text{bf}}(A, \Gamma\Lambda)$ are expressed by occupation probabilities and strengths, whose values are listed in Table I of [35]. The latter are either constant for the entire chain or segments of it, and vary smoothly.

Figures 9(a) and 9(b) show the experimental and calculated levels of selected states in the Nb isotopes along with assignments to configurations based on Eq. (28). In the region between neutron number 50 and 56, there appear to be two sets of levels with quasi-spherical or weakly deformed structure, associated with configurations A and B . All levels decrease in energy for 52–54, away from closed shell, and rise again at 56 due to the neutron $\nu(2d_{5/2})$ subshell closure. From 58, there is a pronounced drop in energy for the states of the B configuration. At 60, the two configuration cross,

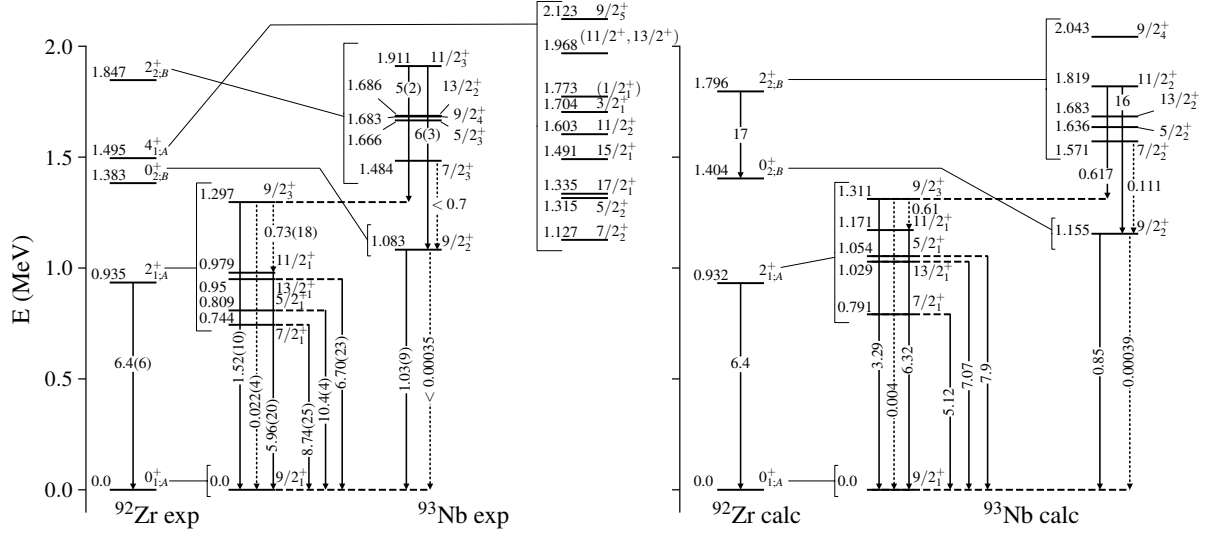


Figure 11: Experimental (left) and calculated (right) energy levels in MeV, and $E2$ (solid arrows) and $M1$ (dashed arrows) transition rates in W.u., for ^{93}Nb and ^{92}Zr . Lines connect L -levels in ^{92}Zr to sets of J -levels in ^{93}Nb , indicating the weak coupling ($L \otimes \frac{9}{2}$) J , Eq. (23). Note that the observed $4^+_{1;A}$ state in ^{92}Zr is outside the $N=1$ model space. Adapted from [35].

indicating a Type II QPT, and the ground state changes from $9/2^+$ to $5/2^+$, becoming the bandhead of a $K = 5/2^+$ rotational band composed of $5/2^+$, $7/2^+$, $9/2^+$, $11/2^+$, $13/2^+$ states. The intruder B configuration remains strongly deformed and the band structure persists beyond 60. A similar trend is encountered in the even-even Zr isotopes with the same neutron numbers, as can be seen in Fig. 4.

3.4 Intertwined QPTs in the Nb chain

Intertwined QPTs are characterized by concurrent Type I and Type II QPTs. Fingerprints of Type II QPT are evident in the evolution of the normal-intruder mixing across the Nb chain. Fig. 10 shows the probability b^2 of the Ψ_B component, Eq. (28), in the wave functions of the ground state (J_{gs}^+) and first-excited state ($7/2^+$), as a function of neutron number. The rapid change in structure of J_{gs}^+ from the normal A configuration at neutron number 52–58 (small b^2 probability), to the intruder B configuration at neutron number 60–64 (large b^2) is clearly evident, signaling a Type II QPT. It should be noted that the ground state angular momentum changes from $J_{gs}^+ = 9/2^+$ in $^{93-99}\text{Nb}$ to $J_{gs}^+ = 5/2^+$ in $^{101-105}\text{Nb}$. Such a possible change is a characteristic signature of Type II QPTs in odd-mass nuclei, unlike even-even nuclei where the ground state remains 0^+ before and after the crossing. The configuration change appears sooner in the $7/2^+$ state, which changes to the B configuration already at neutron number 58. Outside a narrow region near neutron number 60, where the crossing occurs, the two configurations are weakly mixed and the states retain a high level of purity. A glance at Fig. 5(b) shows that such a trend is similar to that encountered for the 0^+ and 2^+ states in the respective ^{40}Zr cores.

Evidence for a Type I QPT, involving shape changes within the intruder B configuration, is obtained by examining the individual structure of Nb isotopes at the end-points of the region considered. Fig. 11 displays the experimental and calculated levels in ^{93}Nb along with $E2$ and $M1$ transitions among them. The corresponding spectra of ^{92}Zr , the even-even core, are also shown with an assignment of each level L to the normal A or intruder B configurations. The latter, as mentioned in Section 2.5, are both spherical or weakly-deformed. The low-lying states of the normal A configuration in ^{93}Nb , can be interpreted in the weak coupling scheme of Eq. (23). Specifically, the coupling of the single-proton $\pi(1g_{9/2})$ state to the $L = 0^+_{1;A}$ ground state of ^{92}Zr , yields the ground state $J = 9/2^+$ of ^{93}Nb . For $L = 2^+_{1;A}$, it yields a quintuplet of states, $5/2^+$, $7/2^+$, $9/2^+$, $11/2^+$, $13/2^+$. A multiplet built on $4^+_{1;A}$ can also be identified in the empirical spectrum of ^{93}Nb . Particularly relevant to the present discussion is the fact that the weak-coupling scheme is also valid for non-yrast states of the intruder B configuration

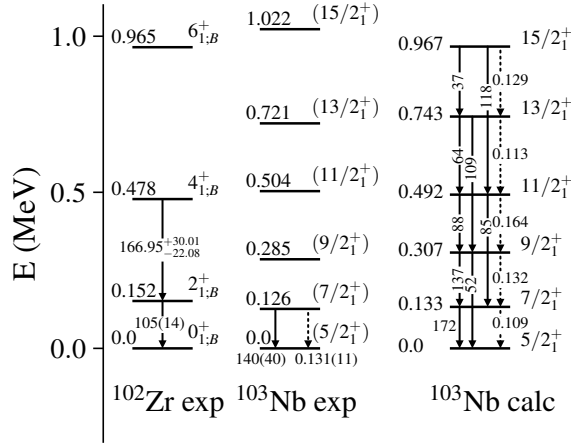


Figure 12: Experimental and calculated energy levels in MeV, and $E2$ (solid arrows) and $M1$ (dashed arrows) transition rates in W.u., for ^{103}Nb and ^{102}Zr .

in ^{93}Nb . As shown in Fig. 11, the coupling of $\pi(1g_{9/2})$ to the $0^+_{2;B}$ state in ^{92}Zr , yields the excited $9/2^+$ state in ^{93}Nb and for $2^+_{2;B}$ it yields the quintuplet of states, $5/2^+_3, 7/2^+_3, 9/2^+_4, 11/2^+_3, 13/2^+_3$.

For ^{103}Nb , the yrast states, shown in Fig. 12, are arranged in a $K = 5/2^+$ rotational band of a prolate-deformed core shape, whose members can be interpreted in the strong coupling scheme of Eq. (24). The indicated states are obtained by coupling the proton $\pi(1g_{9/2})$ state to the ground band ($L = 0^+_{1;B}, 2^+_{1;B}, 4^+_{1;B}, 6^+_{1;B}, \dots$) of the even-even core ^{102}Zr , also shown in Fig. 12, which is associated with the intruder B configuration. The calculations reproduce well the observed particle-rotor $J(J+1)$ splitting, as well as, the $E2$ and $M1$ transitions within the band. Altogether, we see an evolution of structure from weak-coupling of a spherical shape in ^{93}Nb , to strong-coupling of a deformed shape in ^{103}Nb . Such shape-changes within the B configuration (Type I QPT), superimposed on an abrupt configuration crossing (Type-II QPT), are the key defining feature of intertwined QPTs. Interestingly, this intricate scenario, originally observed in the even-even Zr isotopes, persists in the adjacent odd-even Nb isotopes.

3.5 Evolution of observables along the Nb chain

Electromagnetic transitions and moments provide further insight into the nature of QPTs. The quadrupole moment of the ground state J_{gs}^+ and $B(E2; 7/2^+_1 \rightarrow J_{gs}^+)$ in Nb isotopes are shown in Fig. 13(a) and Fig. 13(b), respectively. These observables are related to the deformation, the order parameter of the QPT. Although the data is incomplete, one can still observe small (large) values of these observables below (above) neutron number 60, indicating an increase in deformation. The calculation reproduces well this trend and attributes it to a Type II QPT involving a jump between neutron number 58 and 60, from a weakly-deformed A configuration, to a strongly-deformed B configuration. This behavior is correlated with a similar jump seen for the $B(E2)$'s of $2^+ \rightarrow 0^+$ transitions in the even-even Zr cores, shown in Fig. 6(a), and with the calculated order parameters, shown in Fig. 5(a). A jump in values at neutron number 60 is also seen in the magnetic moment of the ground state ($\mu_{J_{gs}^+}$), shown in Fig. 13(c). The evolution of the two-neutron separation energy (S_{2n}) along the Nb chain, shown in Fig. 13(d), exhibits features of Type I QPTs within the A configuration (B configuration) for neutron number 52-58 (60-64), similar to the behaviour in the even-even Zr isotopes, seen in Fig. 6(c).

4 Concluding remarks

We have presented the notion of intertwined quantum phase transitions (QPTs) and considered its manifestation in a system of bosons and in a mixed system of bosons and fermions. Intertwined QPTs correspond to a situation of a QPT involving the crossing of two (or more) configurations (Type II), each of which is in itself undergoing a QPT (Type I).

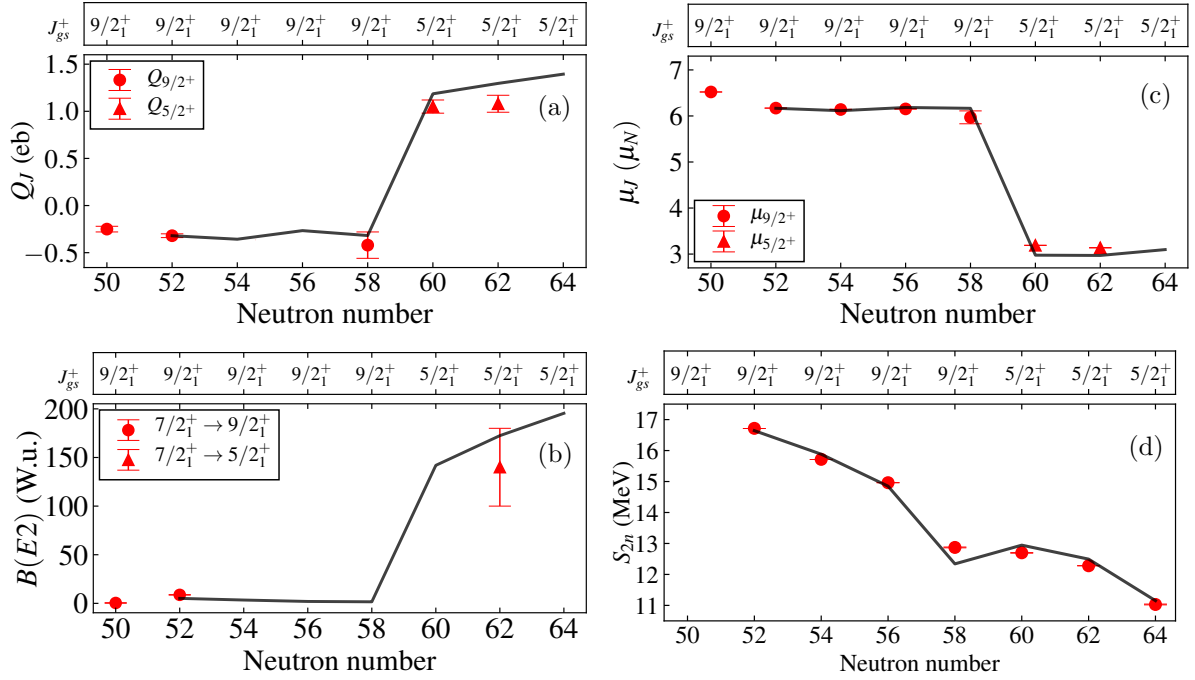


Figure 13: Evolution of observables along the Nb chain. Symbols (solid lines) denote experimental data (calculated results). The values J_{gs}^+ for the ground state are indicated at the top. (a) Quadrupole moments $Q_{J_{gs}^+}$ in e barns (eb). (b) $B(E2; 7/2_1^+ \rightarrow J_{gs}^+)$ in W.u. (c) Magnetic moments $\mu_{J_{gs}^+}$ in μ_N . (d) Two-neutron separation energy S_{2n} in MeV.

As a case study of intertwined QPTs in a finite Bose system, we have employed the algebraic interacting boson model with configuration mixing, describing collective states in even-even nuclei in terms of bosons. A comprehensive analysis of spectral properties of Zr isotopes, including the evolution of structure, order parameters and related observables, revealed the role of two configurations. The normal configuration remained spherical along the Zr chain, while the intruder configuration experienced first a transition from spherical [U(5)] to an axially-deformed [SU(3)] shape, and then a crossover to a γ -unstable [SO(6)] shape. These gradual shape-phase transitions involve a change of symmetries and are superimposed on an abrupt crossing of the two configurations. The normal-intruder mixing is weak (apart from the crossing point), ensuring that both types of QPTs are distinguishable, thus demonstrating intertwined QPTs in even-even nuclei.

As a case study of intertwined QPTs in a finite Bose-Fermi system, we have employed the algebraic interacting boson-fermion model with configuration mixing, which describes low-lying states in odd-even nuclei in terms of ground and core-excited bosonic configurations coupled to a single-fermion. An application to the Nb isotopes disclosed a Type II QPT (abrupt crossing of normal and intruder states) accompanied by a Type I QPT (gradual shape evolution and transition from weak to strong coupling within the intruder configuration), thus demonstrating intertwined QPTs in odd-even nuclei. The observed intertwined QPTs in the odd-mass Nb isotopes echo the intertwined QPTs of the adjacent even-even Zr isotopes.

The results reported in the present contribution motivate further experiments on the spectroscopy of non-yrast states in even-even and odd-even nuclei, as well as set the path for new investigations on multiple and intertwined QPTs in other Bose and Bose-Fermi systems.

Acknowledgments

A fruitful collaboration with N. Gavrielov (GANIL) and F. Iachello (Yale) on the topics considered, is acknowledged.

References

- [1] Gilmore R and Feng D H 1978 *Phys. Lett. B* **76** 26
- [2] Gilmore R 1979 *J. Math. Phys.* **20** 891
- [3] Carr L ed 2011 *Understanding Quantum Phase Transitions* (CRC Press, Boca Raton, FL)
- [4] Cejnar P, Jolie J and Casten R F 2010, *Rev. Mod. Phys.* **82** 2155
- [5] Dieperink A E L, Scholten O and Iachello F 1980 *Phys. Rev. Lett.* **44** 1747
- [6] Heyde K and Wood J L 2011 *Rev. Mod. Phys.* **83** 1467
- [7] Frank A, Van Isacker P and Iachello F 2006 *Phys. Rev. C* **73** 061302(R)
- [8] Gavrielov N, Leviatan A and Iachello F 2019 *Phys. Rev. C* **99** 064324
- [9] Gavrielov N, Leviatan A and Iachello F 2020 *Phys. Scr.* **95**, 024001
- [10] Gavrielov N, Leviatan A and Iachello F 2022 *Phys. Rev. C* **105** 014305
- [11] Iachello F and Arima A 1987 *The Interacting Boson Model* (Cambridge University Press, Cambridge)
- [12] Ginocchio J N and Kirson M W 1980 *Phys. Rev. Lett.* **44** 1744
- [13] Iachello F and Talmi I 1987 *Rev. Mod. Phys.* **59** 339
- [14] Federman P and Pittel S 1979 *Phys. Rev. C* **20** 820
- [15] Heyde K, Van Isacker P, Casten R F and Wood J L 1985 *Phys. Lett. B* **155** 303
- [16] Iachello F and Zamfir N V 2004 *Phys. Rev. Lett.* **92** 212501
- [17] Cejnar P and Jolie J 2009 *Prog. Part. Nucl. Phys.* **62** 210
- [18] Iachello F 2011 *Rivista del Nuovo Cimento* **34** 617
- [19] Macek M and Leviatan A 2014 *Ann. Phys. (N.Y.)* **351** 302
- [20] Duval P D and Barrett B R 1981 *Phys. Lett. B* **100** 223
- [21] Duval P D and Barrett B R 1982 *Nucl. Phys. A* **376** 213
- [22] Frank A, Van Isacker P and Vargas C E 2004 *Phys. Rev. C* **69** 034323 (R)
- [23] Sambataro M and Molnár G 1982 *Nucl. Phys. A* **376** 201
- [24] García-Ramos J E and Heyde K 2014 *Phys. Rev. C* **89** 014306
- [25] Nomura K, Rodríguez-Guzmán R and Robledo L M 2016 *Phys. Rev. C* **94** 044314
- [26] Maya-Barbecho E and García-Ramos J E 2022 *Phys. Rev. C* **105** 034341
- [27] Gavrielov N, García-Ramos J E, Van Isacker P and Leviatan A 2023 *Phys. Rev. C* **108** L031305
- [28] Iachello F and Van Isacker P 1991 *The Interacting Boson-Fermion Model* (Cambridge University Press, Cambridge)
- [29] Scholten O and Blasi N 1982 *Nucl. Phys. A* **380** 509
- [30] Alonso C E, Arias J M, Fortunato L and Vitturi A 2005 *Phys. Rev. C* **72** 061302(R)
- [31] Böyükata M, Alonso C E, Arias J M, Fortunato L and Vitturi A 2021 *Symmetry* **13** 215

- [32] Petrellis D, Leviatan A and Iachello F 2011 *Ann. Phys.* **326** 926
- [33] Nomura K, Nikšić T and Vretenar D 2020 *Phys. Rev. C* **102** 034315
- [34] Leviatan A 1988 *Phys. Lett. B* **209** 415
- [35] Gavrielov N, Leviatan A and Iachello F 2022 *Phys. Rev. C* **106** L051304
- [36] Gavrielov N 2023 *Phys. Rev. C* **108** 014320